

# **The Global Positioning System constellation as a space weather monitor: Comparison of electron measurements with Van Allen Probes data**

Steven K. Morley, John P. Sullivan and Michael G. Henderson

Space Science and Applications, Los Alamos National Laboratory, Los Alamos,  
New Mexico, USA

J. Bernard Blake

Space Science Application Laboratory, Aerospace Corporation, El Segundo,  
California, USA

Daniel N. Baker

Laboratory for Atmospheric and Space Physics, University of Colorado,  
Colorado, USA

---

S. K. Morley, Space Science and Applications, Los Alamos National Laboratory, Mail Stop D466,  
P.O. Box 1663, Los Alamos, NM 87545, USA. (smorley@lanl.gov)

This article has been accepted for publication and undergone full peer review but has not been through the copyediting, typesetting, pagination and proofreading process, which may lead to differences between this version and the Version of Record. Please cite this article as doi: 10.1002/2015SW001339

**Abstract.** Energetic electron observations in Earth’s radiation belts are typically sparse and multi-point studies often rely on serendipitous conjunctions. This paper establishes the scientific utility of the Combined X-ray Dosimeter (CXD), currently flown on 19 satellites in the Global Positioning System (GPS) constellation, by cross-calibrating energetic electron measurements against data from the Van Allen Probes. By breaking our cross-calibration into two parts – one that removes any spectral assumptions from the CXD flux calculation, and one that compares the energy spectra – we first validate the modeled instrument response functions, then the calculated electron fluxes. Unlike previous forward modeling of energetic electron spectra we use a combination of four distributions that, together, capture a wide range of observed spectral shapes. Our two-step approach allowed us to identify, and correct for, small systematic offsets between block IIR and IIF satellites. Using the Magnetic Electron Ion Spectrometer (MagEIS) and Relativistic Electron-Proton Telescope (REPT) on Van Allen Probes as a “gold standard” we demonstrate that the CXD instruments are well-understood. A robust statistical analysis shows that CXD and Van Allen Probes fluxes are similar and the measured fluxes from CXD are typically within a factor of 2 of Van Allen Probes at energies  $\lesssim 4$  MeV. We present data from 17 CXD-equipped GPS satellites covering the 2015 “St. Patrick’s Day” geomagnetic storm to illustrate the scientific applications of such a high data density satellite constellation, and therefore demonstrate that the GPS constellation is positioned to enable new insights in inner magnetospheric physics and space weather forecasting.

Index terms: Radiation belts; Energetic particles: trapped; Space radiation environment; Instruments and techniques

Key points.

1. The CXD instruments have been cross-calibrated against Van Allen Probes.
2. CXD and Van Allen Probes fluxes are typically within a factor of 2 from about 140 keV - 4 MeV.
3. The 19 CXD-equipped GPS satellites provide high fidelity measurements and high data density.

## 1. Introduction

The outer electron radiation belt is located on closed drift paths at radial distances typically between 3.5 and 7 Earth radii ( $R_E$ ) [e.g. *Ganushkina et al.*, 2011]. This environment is highly dynamic and largely driven by variations in the solar wind [e.g. *Li et al.*, 2005]. Understanding the dynamics of the Van Allen radiation belts is not only of scientific importance, but the acceleration and loss processes that govern the dynamics can have significant effects on, among others, technological assets in space [*Baker*, 2000; *Welling*, 2010; *Lohmeyer and Cahoy*, 2013] and atmospheric chemistry relevant to climate [*Turunen et al.*, 2009; *Rozanov et al.*, 2012].

Since the launch of the Van Allen Probes mission [*Mauk et al.*, 2013] significant progress has been made in understanding the acceleration of lower energy “seed” electrons up to relativistic energies [*Reeves et al.*, 2013], and rapid losses of radiation belt electrons [*Turner et al.*, 2014].

This latter study combined energetic electron data from eight satellites; however the use of a “virtual constellation” like this still relies on serendipity due to the interplay of the orbits of the constituent spacecraft. Energetic particle detectors developed by Los Alamos National Laboratory (LANL) have been flown in Medium Earth Orbit (MEO) on the Global Positioning System (GPS) constellation for more than 2 decades; at the end of August 2015 there were 21 active GPS satellites equipped with energetic particle sensors.

The original GPS Burst Detection Dosimeter (BDD) series [*Drake et al.*, 1993] saw limited scientific application [e.g. *Ingraham et al.*, 1996]. The subsequent series of GPS particle detectors, BDD-II [*Feldman et al.*, 1985], has seen much wider scientific use [e.g. *Li et al.*, 1999; *McAdams et al.*, 2001; *Vassiliadis et al.*, 2003; *Taylor et al.*, 2004; *Bourdarie et al.*, 2005; *Maget et al.*, 2007; *Millan et al.*, 2007; *Ginet et al.*, 2013], primarily to characterize the dynamics of the

radiation belt at  $L \sim 4$ . These detectors suffered from drifts in the gain, leading to varying energy thresholds and efficiencies throughout their lifetimes [Friedel *et al.*, 2005]. By intercalibrating these detectors with the Combined Release and Radiation Effects Satellite's (CRRES) magnetic electron spectrometer [Vampola *et al.*, 1992], LANL's Synchronous Orbit Particle Analyzer (SOPA) [Belian *et al.*, 1992; Cayton and Tuszewski, 2005] and the Comprehensive Energetic Particle Pitch Angle Distribution (CEPPAD) instrument on Polar [Blake *et al.*, 1995], Friedel *et al.* were able to adjust the energy channel assignments and derive "correction factors" for the estimated electron fluxes. Through this procedure the utility of the BDD-II data for scientific use was clearly established.

Since late 2000, two new series of instrument have been flown on the GPS constellation: The BDD-IIR detector [Cayton *et al.*, 1998], which is significantly different to the BDD-II described above; and the Combined X-ray Dosimeter (CXD), which is an entirely new design [Cayton, 2004; Tuszewski *et al.*, 2004].

Figure 1 shows the temporal coverage of the energetic electron detectors flown on the GPS constellation from July 1990 to August 2015. The daily sunspot number is given by the dark grey line to show the context within the solar cycle. The colored horizontal bars show the data coverage for each satellite. The dark blue bars show the "gold standard" radiation belt missions: CRRES (1990-1991) and Van Allen Probes (2012-). The red bars mark the coverage of the CXD-equipped GPS satellites, details of which are given in table 1. The green bars mark the coverage of the BDD-IIR instrumented GPS satellites and the cyan bars show the coverage of the older BDD-II series detectors.

In this manuscript we will discuss the CXD instruments as they are well-understood and their performance has not previously been adequately addressed in the literature. The CXD

instruments are the most numerous of the particle sensors on the GPS constellation, are well-intercalibrated, and have been used for recent radiation belt studies [Morley *et al.*, 2010a, b; Yu *et al.*, 2013]; while similar work is ongoing for the BDD-IIR flux data, which have been used extensively by the Dynamic Radiation Environment Assimilation Model [e.g. Koller *et al.*, 2007; Reeves *et al.*, 2012], we restrict this manuscript to discussing CXD. This paper will describe the temporal and spatial coverage of the CXD-equipped GPS constellation (hereafter just referred to as GPS), before comparing GPS electron measurements with coincident data from the Van Allen probes Energetic Particle, Composition, and Thermal Plasma (ECT) suite [Spence *et al.*, 2013] to demonstrate the quality and utility of the GPS data for space weather science. This paper will conclude with a look at the radiation belt dynamics for the “St. Patrick’s Day” storm (onset on March 17th, 2015) using GPS data, and compare to the storm-time evolution of the radiation belts observed by the Van Allen Probes, to illustrate the utility of a high data density satellite constellation.

## **2. Data Description**

### **2.1. Data Sources and Coverage**

The GPS satellites are distributed across six orbital planes and follow near-circular orbits, with a 12 hour period, at an altitude of approximately 20200 km. The six orbital planes are distributed around the Earth and are nominally inclined at 55 degrees. A visualization of the orbits of the CXD-equipped GPS satellites is shown in figure 2, at midnight on March 17th 2015, in Geocentric Solar Ecliptic (GSE) coordinates. The satellite names mark the location of each satellite at this time and the orbital track for the previous 12 hours is shown in color. The colors fade with both distance from the viewpoint and with “age” of the point. The orange and red arrows mark the Earth-Sun vector and GSE X-vector, which are identical in the GSE

system. The GSE Z-vector is marked by the blue arrow and the green arrow marks the dipole axis.

The most common energetic particle instrument on the GPS platform is the Los Alamos National Laboratory Combined X-ray Dosimeter (CXD). The CXD instrument measures energetic electrons with two sensors: the Low Energy Particle (LEP) sensor, which provides five electron energy channels from about 140 keV; and the High Energy Particle (HXP) sensor, which provides six electron energy channels from about 1.3 MeV upwards. Nominal energies for these channels are given in table 2. Various sampling rates can be commanded, though the typical sampling rate is 240 s. Each of these sensors also provides proton measurements, and the proton data will be the subject of future work. Details of the instrument design, including the integrated X-ray sensors, are given by *Distel et al.* [1999] and more details on the LEP sensor are given by *Tuszewski et al.* [2004].

The Van Allen Probes satellites are in highly elliptical, low-inclination orbits. The orbits are configured slightly differently, such that one spacecraft laps the other spacecraft several times per year. We use energetic particle data from the Magnetic Electron Ion Spectrometer [MagEIS; *Blake et al.*, 2013] and the Relativistic Electron Proton Telescope [REPT; *Baker et al.*, 2013]. Full details of the Van Allen Probes mission and orbital configuration can be found in *Mauk et al.* [2013] and descriptions of the energetic particles suite are given by *Spence et al.* [2013, and references therein]. Additional work discussing on-orbit calibration and cross-calibration of the Van Allen Probes instruments has been presented by *Morley et al.* [2013] and *O'Brien et al.* [2015].

As shown in figure 1, by the end of August 2015 there were 19 GPS vehicles in orbit equipped with CXD instrument packages – these are the satellites we have used for this study – giving

~118 satellite-years of CXD data since 2001; the two GPS vehicles equipped with BDD-IIR sensors will be addressed in future work. We will identify the satellites by their SVN (satellite vehicle number) for consistency with previous work [e.g. *Taylor et al.*, 2004; *Morley et al.*, 2010b; *Ginet et al.*, 2013]. Selected details of the satellites used in this study are given in table 1. Figure 3a shows the range of magnetic local times (MLT) sampled by GPS vehicle ns65 between September 2012 and August 2015, as a function of L. Figure 3b shows the orbital coverage of ns65 in magnetic latitude (MLat) as a function of L. The L used here is the McIlwain L [*McIlwain*, 1961; *Hilton*, 1971] for a locally mirroring particle; MLat and MLT are calculated for an eccentric dipole [*Fraser-Smith*, 1987]. It should be noted that the GPS satellites, which are in near-circular orbits, sample a range of magnetic latitudes due to the inclination of their orbit and hence also sample a wide range of L. This characteristic orbit therefore restricts the range of equatorial pitch angles sampled by the satellites as a function of L - as the magnetic latitude increases, the maximum equatorial pitch angle that is observable decreases. Figure 3d follows the same format, but shows the MLat-L coverage for a Van Allen Probes satellite (RBSP-A) between September 2012 and August 2015. The coverage is calculated from daily files of the magnetic coordinates of each satellite at 5 minute cadence and, to reduce the number of samples, 200 days are randomly selected from the full data interval. The probability of occurrence of a given L-MLat bin is then calculated from the reduced data set. Figure 3d is the same as figure 3b, but for RBSP-A.

## 2.2. Conjunctions between GPS and Van Allen Probes

A physical conjunction between a GPS satellite and one of the Van Allen probes (both A and B were used) was defined whenever the Euclidean distance between them falls below 1000km. To calculate the distance between the GPS satellites and Van Allen probes satellites we have



used ephemeris data at 1-minute cadence, and where a conjunction is found the nearest CXD electron data point is taken as the time of conjunction. As the CXD data are sampled at 240 s cadence, we exclude any additional conjunctions that may fall in this time window. Adjacent data points in the ephemeris can therefore yield multiple conjunctions that are separated in time by 4 minutes. The set of conjunctions includes 48 that are separated from the previous conjunction by 4 minutes; only two sets of conjunctions contain more than two adjacent measurements. Across the interval of study (September 2012 to August 2015) we have identified 140 conjunctions between CXD-equipped GPS and Van Allen Probes. As the MagEIS and REPT data used are at the cadence of the Van Allen Probes spin period ( $\simeq 10$  s) we then average the Van Allen Probes data for the sampling interval for each CXD observation. Due to the phasing of the orbits and the temporal coverage of the satellites, the majority of conjunctions are on the nightside, however their distribution in latitude is fairly even. The median Kp value for all conjunctions is  $1^+$  and the upper and lower quartiles are ( $3^-$ ,  $1^-$ ); the peak Kp value at any conjunction is  $5^+$ . The median Dst value for all conjunctions is  $-7$  nT and the upper and lower quartiles are (4,  $-17$ ) nT; the minimum Dst value at any conjunction is  $-72$  nT. The set of conjunctions therefore represents a wide range in geomagnetic activity levels.

### **3. Results**

#### **3.1. Comparison between GPS and Van Allen Probes MagEIS/REPT**

To show how well the GPS detectors perform we compare to the Van Allen Probes ECT suite (MagEIS and REPT). In the first instance we remove spectral assumptions inherent in the GPS flux calculation [Morley *et al.*, 2014] by combining the Van Allen Probes fluxes with the GPS instrument response functions ( $G(E)$ ), as described by equation 1. This gives us the expected count rate ( $C$ ) in the GPS detector, assuming the flux measurements from the Van Allen Probes

$j(E)$ ) as our ground truth. Each energy channel of the detector is analyzed in this way and we perform our initial analysis using these data. The CXD instrument response function is calculated from Monte Carlo simulation [e.g. *Cayton, 2004; Morley et al., 2014*], and this can be regarded as an energy-dependent geometric factor.

$$C_i = \int_E j(E) G_i(E) dE \quad (1)$$

Figure 4 shows, in the left panel, the differential number fluxes measured by the MagEIS and REPT instruments on the Van Allen Probes satellite RBSP-A at a physical conjunction between RBSP-A and ns59. In the right hand panel the expected counts (calculated from the RBSP-A data) and the observed counts (measured by the CXD on ns59) are shown. The right-hand panel is annotated with metrics for the correspondence between the count rates; the mean error ratio  $\epsilon$  is defined to be the mean ratio of CXD counts to “expected” counts. The data shown in figure 4 have been calculated for 140 conjunctions between GPS and the Van Allen Probes.

To investigate the correspondence for each energy channel of CXD, figure 5 presents scatter plots for the first four energy channels of the GPS detectors. Data from energy channels five through eight are shown in an identical format in figure 6. The abscissa is the count rate observed by GPS and the ordinate is the expected count rate, based on ECT flux data. A dashed black line corresponding to  $y = x$  has been added to each plot. A line of best fit on  $\log_{10}$  counts has been calculated using ordinary least squares (OLS), shown in red, and a 95% confidence interval on the fitted line is shown by the grey shading [see, e.g. *Sheskin, 2007*, pp. 1241-1243]. Each panel is annotated with the Pearson correlation coefficient ( $R$ ) and the coefficient of determination ( $R^2$ ) for the linear fit. Taking the  $\log_{10}$  prior to fitting is a necessary step for a statistically valid analysis; among other motivations, we hereby reduce the heteroskedasticity of the data allowing application of OLS. To avoid comparing background count rates, which

would not be expected to follow a linear model, where the CXD count rate falls below  $2\text{ s}^{-1}$  we have removed the data from this analysis. This filter only affects three conjunctions for channels 1-6, with the number of points excluded rising to 25 by channel 8.

The same information is encapsulated in Figure 7, in the form of boxplots. A boxplot is shown for each electron energy channel on GPS, and the ordinate is the  $\log_{10}$  ratio of observed count rate to expected count rate. We use the  $\log_{10}$  of the ratio so that the ratios are symmetric both above and below 1. To make this figure easier to interpret we have included a dark grey shaded area that marks a factor of 2 difference, and a light grey shaded area that marks a factor of 3 difference. The central box marks the inter-quartile range, thus containing the middle 50% of the data, and the red bar locates the median value; the notches surrounding the red bar mark a bootstrapped 95% confidence interval about the median. The bars (“whiskers”) extend to 1.5 times the interquartile range beyond the upper and lower quartiles [cf. *Tukey*, 1977; *Wilks*, 2006]. Any points outside of the whiskers are deemed to be outliers and are marked individually. By comparing the boxplots for each electron energy channel it is easily seen that the typical observed count rate is close to the expected count rate (the 95% CI on the median includes unity) and only a small fraction of comparisons are more than a factor of two different. This figure also includes boxplots for energy channels 9, 10 and 11. While the median ratio for channel 9 is close to unity, the spread (as measured by the inter-quartile range) is larger than lower energy channels; the counts in channels 10 and 11 do not compare at all well to the counts expected from the Van Allen Probes energy spectrum, but as these channels measure electron energies greater than  $\sim 4\text{ MeV}$  this is most likely due to unaccounted-for instrument backgrounds.

The largest outlier seen in CXD channels 1 and 2 has been investigated. For this work we have used the background-corrected MagEIS fluxes [see *Claudepierre et al.*, 2015] and where no background correction is available the flux is set to a fill value; we note that this primarily affects the lower energy channels on RBSP-A. In this case our processing sets the missing MagEIS flux values to zero and thus the “expected” count rate is underestimated in the channels most sensitive to lower energy electrons. The outlier is a case where the background correction could not be applied and no MagEIS data below 1 MeV were used. To improve the comparison between the “expected” and observed count rates we could either ignore these cases or fill the spectrum with the uncorrected MagEIS fluxes. Since only a small fraction of the conjunctions are affected by fill values in the corrected MagEIS data we have chosen to leave them in our analysis, but noting that the largest differences between the lower energy channels on CXD and Van Allen Probes data can be explained.

### **3.2. CXD electron fluxes**

Until this point, we have been comparing counts from the CXD instruments with “expected counts” obtained by folding the RBSP flux spectrum through the GPS instrument responses. While this demonstrates that the instrument is indeed well understood, the inversion of the counts to flux is not trivial. In this section we therefore provide a brief overview of the current forward modeling methodology for deriving fluxes and compare these derived data with Van Allen probes flux data.

Full details of the data processing methodology for GPS are given by *Morley et al.* [2014], though for this work we have extended the forward model as described below. As described in *Morley et al.* [2014], we account for the response in the electron channels due to protons when fitting energy spectra. As noted previously the response matrix is calculated from Monte Carlo

simulation with a distribution of incident particle energies [Cayton, 2004; Morley *et al.*, 2014], and can be regarded as an energy-dependent geometric factor. The instrument response is then multiplied by an assumed energy spectrum for a wide range of possible parameter space. The fitting process adopted during this work assumes three Maxwell-Jüttner (relativistic Maxwellian) distributions, with the addition of a normal distribution (in  $\log(\text{momentum})$ ) to allow the fit to capture a localized peak in the energy spectrum; the use of Maxwellians in fitting energetic electron data has been discussed by, among others, Cayton *et al.* [1989], Borovsky *et al.* [1998] and Cayton and Tuszewski [2005]. The specific application (of a single relativistic Maxwellian) to GPS data has been discussed by Denton and Cayton [2011], along with limitations of using a single relativistic Maxwellian [see also Morley *et al.*, 2014]. We use a nonlinear optimization to find the best-fit parameters for each component distribution, and using four components allows us to flexibly capture observed energy spectra without overfitting. Additional details are given in the Appendix.

While performing this work systematic offsets between the expected and observed counts were found, in particular for the lowest 5 energy channels. These energy channels are from the low-energy particle (LEP) component of the CXD instrument [Cayton, 2004] and the sense of the offset was consistent with an underestimate of the Bremsstrahlung contribution [Tuszewski *et al.*, 2004]. A constant scaling was applied to the Bremsstrahlung component of the instrument response, which was found to improve agreement with the “expected” counts, however, applying a constant scaling to the full energy-dependent response both improved the median error and reduced the spread of count ratios. We therefore revised the response functions, using constant scaling factors which are given in table 2), to cross-calibrate the CXD instruments with the Van Allen Probes ECT suite, but we again note that the scaling factors are small and

previous work using CXD-derived fluxes [e.g. *Yu et al.*, 2013] is unaffected by this change. All results presented in this paper use the revised instrument response functions.

Figure 8 shows six sample comparisons of flux spectra at conjunction times. The sample spectra were selected to be representative of the typical quality of fit across a range of spectral forms. We note that the upper right panel shows the fitted spectrum for the conjunction shown in Figure 4. Each panel shows the fitted differential flux spectrum estimated using the GPS count rate data as the solid black line. The component spectra are shown in different colors and linestyles: the Maxwell-Jüttner distributions are shown in magenta (with crosses), red (dashed) and green (with diamonds); the Gaussian distribution is shown in cyan (dash-dot). The pair of satellites in conjunction are listed in the title for each panel, along with the date and time of the conjunction. The Van Allen Probes spectrum is a average flux spectrum for the 4-minute sampling interval centered on the nominal CXD sample time.

Flux spectra have been calculated for all 140 conjunctions and we follow the approach in section 3.1 to assess the correspondence between the CXD flux measurements and the Van Allen Probes flux data. Figure 9 shows scatter plots of the CXD flux against the Van Allen Probes flux at selected energies between 350 keV and 3.4 MeV. The panels follow the format of 5, but have different information in the annotation and an additional linear fit. Each panel is annotated with the energy, the median flux ratio, the Pearson correlation coefficient ( $R$ ) and the coefficient of determination ( $R^2$ ). We define the median flux ratio is calculated as,  $M = \text{median}(j_{CXD}/j_{RBSP})$ , thus a median ratio greater than unity indicates that CXD fluxes are typically higher than Van Allen Probes fluxes at that energy. Similarly, a median ratio less than unity indicates that CXD fluxes are typically lower than Van Allen Probes fluxes. A median ratio of unity would indicate that the measurements are typically the same and are thus unbiased. The

linear fit given by the red line (with grey 95% CI) in figure 9 is as described for figure 5; the additional linear fit marked by the purple line (with a yellow 95% CI) is a robust linear fit using the Theil-Sen estimator [Sen, 1968; Wilcox, 1998].

At lower values of flux, the correspondence between CXD and Van Allen Probes is not as good; that is, the deviation from a model  $j_{CXD} = j_{RBSP}$  increases at lower fluxes. Ordinary least squares (OLS) regression is not robust to outliers [e.g. Wilks, 2006], and though the bulk of data points are at higher flux the outliers at low flux can significantly affect the OLS fit. To examine the effect of the low flux cases on the best-fit linear model we have used the Theil-Sen estimator to provide a robust linear regression. This estimator is calculated as the median of all slopes calculated from all pairings of data points. As such it is robust to outliers, but is an unbiased estimator of the true slope [Sen, 1968]. The panels in figure 9 corresponding to energies of 0.35 MeV, 0.73 MeV and 3.4 MeV all have a Theil-Sen line where the CI encompasses the  $y = x$  line, in contrast to the OLS fit which can be seen to be affected by points at low flux. The slopes and CIs for at 1.55 MeV and 2.6 MeV are similar for both methods and the 1.55 MeV fit is consistent with a model of  $j_{CXD} = j_{RBSP}$ . The slopes of the best linear models at 1.0 MeV and 2.6 MeV are very close to 1, but display a systematic offset such that CXD consistently underestimates the fluxes by factors of up to 2. These systematic offsets are better understood by displaying these data as boxplots.

Figure 10 shows the distributions of flux ratios at twelve different energies, from 230 keV up to 5.2 MeV, as box plots. For symmetric representation of ratios about 1, see section 3.1, we plot the logarithm of the flux ratio ( $\log_{10}(j_{CXD}/j_{RBSP})$ ). The box plots follow the same format as in Figure 7. The median flux ratios are within a factor of two from 230 keV to 4.2 MeV, and the median CXD flux at 5.2 MeV is within a factor of 3 of Van Allen Probes, though the spread is

large. Across this set of conjunctions there are clear differences between the flux measurements from CXD and Van Allen Probes, but these vary with energy and are typically much less than a factor of two. For most sampled energies the majority of conjunctions yield results that lie within a factor of two of the Van Allen Probes measurement. Taking the 1.0 MeV comparison as our “worst case” example, we can see that 50% of the data are within a factor of two of the Van Allen Probes data, and more than 75% are within a factor of three. In the 5.2 MeV energy channel CXD is systematically much lower than RBSP; we use the CXD proton flux to estimate the background due to protons in the electron channel and subtract this prior to estimation of the electron fluxes. Although the REPT background is known to be low, there is no explicit background subtraction performed in the data used for this work, and hence the CXD fluxes at this energy are expected to be lower.

The largest typical disagreements are seen around 1-2 MeV and the most likely reason for this can be seen in Figure 8. In several of these spectra the Van Allen Probes data display a clear peak in this energy range. These spectral types are consistent with observations from CRRES inside the plasmopause [Johnston *et al.*, 2010, ; also W.R. Johnston, C.D. Lindstrom and G.P. Ginet, “Characterization of radiation belt electron energy spectra from CRRES observations”, manuscript in preparation for Geophysical Research Letters, hereafter referred to as Johnston *et al.*, 2015]. Johnston *et al.* [2015] also showed that outside the plasmopause the spectral shape was typically better described by exponential and power-law fits with the spectrum typically hardening at higher L [see also Cayton *et al.*, 1989]. Based on this we believe it is reasonable to suppose that the fitting procedure will better capture the spectral shapes typically observed at higher L, with the results presented here representing a “worst case”.



### 3.3. Sample Event: March 17th, 2015 storm

Now that the correspondence between GPS-derived fluxes and Van Allen Probes fluxes has been demonstrated, we turn to illustrating the utility of the Global Positioning System as a space environment monitor. First we note the major caveats associated with flux data from the CXD instrument: CXD does not provide pitch-angle resolved measurements; due to the orbital inclination the equatorial pitch angles sampled near  $L \simeq 6.6$  are typically in the range  $20^\circ$ - $30^\circ$ , with the full range of equatorial pitch angles sampled only as each GPS satellite crosses the magnetic equator near  $L \simeq 4$ . We note also that, although Van Allen Probes is “near-equatorial”, the magnetic latitude can be up to  $\pm 20^\circ$  and therefore Van Allen Probes can also be unable to measure equatorial pitch angles above  $30^\circ$ . Referring to figures 3b and 3d we can see that while this situation is always the case for GPS, the Van Allen Probes are more typically near the magnetic equator and will measure the majority of equatorial pitch angles.

By combining data from seven GPS satellites, *Morley et al.* [2010a] were able to obtain nearly complete coverage of the radiation belts at hourly temporal resolution. They used this unprecedented data density to analyze a rapid dropout of the electron radiation belt in May 2007 and determine timescales for the dropout at different L and energy, finding that the dropout occurred in less than 2 hours (for  $E \leq 1.25$  MeV). As the number of GPS satellites equipped with CXD instrumentation has increased dramatically in recent years we are now able to combine many more satellites and further improve our data coverage. Figure 11 shows electron flux data at 1 MeV from GPS (upper panel), and Van Allen Probes (lower panel), for a week in March 2015. The data presented are binned averages, where the bins are 20 minutes in time and  $\frac{1}{3}$  in L; data from 17 GPS satellites are included in the upper panel, both RBSP-A and RBSP-B are included in the lower panel. The L value used here is the McIlwain L for locally

mirroring particles, calculated using the T89 magnetic field model [Tsyganenko, 1989]. The outer edge of the GPS data is determined by two factors: First, a spectral fit is not determined in cases where the estimated background is high relative to the count rates (the count rate must exceed the background rate plus  $3\sigma$ , where  $\sigma$  is the estimated standard deviation for a Poisson process); second, if the field line is open for a given location then a McIlwain L value cannot be determined and the data will not be included. The Van Allen Probes data displayed are spin-averaged fluxes from MagEIS – to maximize data availability we present MagEIS data that has not been background-corrected in this figure.

The interval plotted contains the “St. Patrick’s day” storm of 2015, which began on March 17th. For an overview of this event the reader is referred to *Cherniak et al.* [2015], particularly their figure 1. The main features of the radiation belt dynamics – a rapid and deep dropout, followed by a long period of strongly enhanced electron flux – can be clearly identified in both data sets. As we are averaging over local time, and bearing in mind the caveats given above, we do not expect identical estimated fluxes for any given L and time. Though the capabilities of the ECT instrument suite are clearly superior to CXD, as figure 11 demonstrates the data density allow science discovery that is impossible with Van Allen Probes alone. The 20 minute resolution of the displayed GPS data are sufficient to resolve the rapid flux dropout at low L, with the flux at  $L \simeq 4.1$  falling by a factor of  $\sim 20$  over  $< 3$  hours. Outside  $L \simeq 5$  the counts fall rapidly to background in the CXD instruments and so no fluxes are calculated, however we note that the *Shue et al.* [1997] magnetopause model predicted a minimum magnetopause standoff of  $5 R_E$  (not shown). A detailed analysis of this storm is planned, but is beyond the scope of the current work. The key point is that the unprecedented number of identically instrumented GPS

satellites will provide valuable context for current and future science missions, while enabling scientific discovery and space weather monitoring in its own right.

The potential impact of these data is wide-ranging, including data assimilation for reanalysis [e.g. *Reeves et al.*, 2012; *Kellerman et al.*, 2014], further development of climatological models [*Ginet et al.*, 2013], and detailed analysis of radiation belt dynamics [*Morley et al.*, 2010a]. As recently noted by *Horne and Pitchford* [2015], satellites being moved to geosynchronous orbit by means of electric orbit raising will move through the heart of the radiation belts for 200-400 days. This argues strongly for an increased understanding, and situational awareness, of the medium-Earth orbit radiation belt dynamics.

#### **4. Summary and Conclusions**

Using the Van Allen Probes ECT suite as a “gold standard” we have assessed our understanding of the CXD energetic particle instrument, currently flown on more than 18 Global Positioning System satellites, and have validated our calculation of differential number flux.

We find that:

1. The CXD instruments are well understood as demonstrated by the comparison between the observed count rate and an “expected” count rate derived using Van Allen Probes flux data and the CXD instruments response functions.
2. The original instrument response functions presented by *Cayton* [2004] [see also *Morley et al.*, 2014] allowed good estimation of the CXD count rates from Van Allen Probes flux data, but small systematic biases (given in table 2) were found in the responses of block IIR and block IIF satellites. The instrument response functions have been modified to cross-calibrate the CXD instruments against the Van Allen Probes ECT suite.

3. The CXD instruments provide good quality measurements of the electron number flux from energies of about 140 keV to about 4 MeV. Robust linear regression shows that the CXD and Van Allen Probes fluxes at conjunction are well-modeled by a straight line with a slope near

1. The measured fluxes from CXD are typically within a factor of 2 of the flux measurements from Van Allen Probes.

4. We have established the scientific utility of the CXD energetic particle sensors on the GPS constellation and argue that using physical conjunctions near  $L=4$  represent a worst case; flux estimates at higher  $L$  are likely to have a smaller error in their estimation due to the spectral shape being more exponential. By demonstrating the high fidelity electron flux measurements available from the GPS constellation, we believe this data set is now positioned to provide new insights in space weather nowcasting, scientific understanding of energetic electron processes and further development of statistical radiation belt models such as AE9/AP9/SPM [Ginet *et al.*, 2013].

#### **Appendix: Flux fitting procedure**

The fit function has three relativistic Maxwellian (Maxwell-Jüttner; hereafter referred to as MJ) components plus a Gaussian term in  $\log(\text{momentum})$ . The procedure we have adopted for fitting is iterative: fits are done in series, adding one function at a time until the final step fits all four components simultaneously.

We define our component distributions as follows, where the normalizations for each distribution are denoted by  $N$  and the differential number flux is denoted by  $j$ . The subscripts  $MJ$

and  $G$  refer to the MJ and Gaussian distributions, respectively.

$$N_{MJ} = \frac{n_i c}{4\pi T K_2(m_e/T)} \quad (2)$$

$$j_{MJ} = N_{MJ} \frac{p^2}{\exp(m_e/T) m_e^2} \exp(-E/T) \quad (3)$$

$$j_G = N_G \left( \frac{\ln(p/\mu)^2}{2\sigma^2} \right) \quad (4)$$

where  $p^2 = (E + m_e)^2 - m_e^2$ ,  $E$  is the electron kinetic energy,  $m_e$  is the electron rest mass energy (0.511 MeV),  $T$  is the temperature of the distribution,  $n$  is the number density and  $\mu$  is the relativistic momentum at the peak of the Gaussian distribution.  $K_2$  is a modified Bessel function of the second kind, of order 2.

The initial values for minimization are taken from the single-component MJ fit described in *Morley et al.* [2014]. All subsequent fitting is performed using the MINUIT minimization package [*James and Roos*, 1975] with the ROOT data analysis framework [*Antcheva et al.*, 2009]. The specific minimization algorithm used is the MIGRAD algorithm, which is a variant of the Davidon-Fletcher-Powell method [e.g. *Press et al.*, 1992]. We use the fit parameters  $n_0$  and  $T_0$  as the initial guess for a constrained fit of the first MJ component. The number density and temperature of the resultant distribution are constrained to lie in the interval

$$\frac{n_0}{10} < n'_0 < 10n_0 \quad (5)$$

$$\frac{T_0}{3} < T'_0 < 3T_0 \quad (6)$$

The resulting parameters are  $n'_0$ , and  $T'_0$ , which are used for constraining later stages in the fitting. We then set the limits for the first two MJ distributions to be:

$$0.1n'_0 < n_1 < 5n'_0 \quad (7)$$

$$T'_0/3 < T_1 < 3T'_0 \quad (8)$$

$$0 < n_2 < 10n'_0 \quad (9)$$

$$3.3T'_0 < T_2 < \max(15T'_0, 10 \text{ MeV}) \quad (10)$$

The initial guesses for the parameters of the first MJ are  $n'_0$  and  $T'_0$ , and for the second MJ are  $n_2 = n'_0/10$  and  $T_2 = 5T'_0$ . A four-parameter fit is then performed, fitting all four parameters simultaneously, and all parameters are allowed to vary within the constraints given above.

Now we add a third MJ distribution with parameters  $n_3$  and  $T_3$  and initial guesses of  $n_3 = n_1/10$  and  $T_3 = T_1/5$ , with limits:

$$0 < n_3 < 3 \cdot \max(n_1, n_2) \quad (11)$$

$$T'_0/33 < T_3 < T'_0/3.3 \quad (12)$$

Constraints on the other parameters are the same as given previously. The full fit is then redone with 3 MJ distributions simultaneously, allowing all  $n$  and  $T$  parameters to vary within constraints.

The last step in the fit procedure is to add a Gaussian in log of momentum with three parameters  $N_G$ ,  $\mu$  and  $\sigma$ . Initial guesses are  $N_G = 1000 \text{ cm}^{-2} \text{ sr}^{-2} \text{ sec}^{-1} \text{ MeV}^{-1}$ ,  $\mu = 2 \text{ MeV}/c$  and  $\sigma = 0.3$  with limits:

$$0 < N_G < 1e8 \quad (13)$$

$$0.6 < \mu < 10 \text{ MeV}/c \quad (14)$$

$$0.2 < \sigma < 2 \quad (15)$$

Finally all nine parameters are fit simultaneously, with the aforementioned constraints, to give the final fit parameters for the four component distributions. The final flux spectrum is therefore the linear sum of these four distributions.

**Acknowledgments.** This work was performed under the auspices of the US Department of Energy and was funded by the Laboratory Directed Research and Development (LDRD) program. We thank W. R. Johnston (Air Force Research Laboratory) for helpful discussions. Analysis and plotting used the publicly available ROOT, LANLGeoMag and SpacePy libraries. Sunspot data are from the World Data Center SILSO, Royal Observatory of Belgium, Brussels (<http://www.sidc.be/silso/datafiles>). Orbital elements for GPS were obtained from <http://www.Space-Track.org>. Both ephemeris data for Van Allen Probes and MagEIS/REPT data were obtained from <http://www.rbsp-ect.lanl.gov>. All MagEIS and REPT data used were from “release 3”. The CXD data used are available on request from the authors.

## References

- Antcheva, I., M. Ballintijn, B. Bellenot, M. Biskup, R. Brun, N. Buncic, P. Canal, D. Casadei, O. Couet, V. Fine, L. Franco, G. Ganis, A. Gheata, D. G. Maline, M. Goto, J. Iwaszkiewicz, A. Kreshuk, D. M. Segura, R. Maunder, L. Moneta, A. Naumann, E. Offermann, V. Onuchin, S. Panacek, F. Rademakers, P. Russo, and M. Tadel (2009), ROOT – a C++ framework for petabyte data storage, statistical analysis and visualization, *Computer Physics Communications*, 180(12), 2499 – 2512, doi:10.1016/j.cpc.2009.08.005.
- Baker, D., S. Kanekal, V. Hoxie, S. Batiste, M. Bolton, X. Li, S. Elkington, S. Monk, R. Reukauf, S. Steg, J. Westfall, C. Belting, B. Bolton, D. Braun, B. Cervelli, K. Hubbell, M. Kien, S. Knappmiller, S. Wade, B. Lamprecht, K. Stevens, J. Wallace, A. Yehle,

H. Spence, and R. Friedel (2013), The Relativistic Electron-Proton Telescope (REPT) instrument on board the Radiation Belt Storm Probes (RBSP) spacecraft: Characterization of Earth's radiation belt high-energy particle populations, *Space Science Reviews*, 179(1-4), 337–381, doi:10.1007/s11214-012-9950-9.

Baker, D. N. (2000), The occurrence of operational anomalies in spacecraft and their relationship to space weather, *IEEE Trans. Plasma Sci.*, 28, 2007–2015, doi:10.1109/27.902228.

Belian, R. D., G. R. Gisler, T. Cayton, and R. Christensen (1992), High-Z energetic particles at geosynchronous orbit during the great solar proton event series of October 1989, *Journal of Geophysical Research: Space Physics*, 97(A11), 16,897–16,906, doi:10.1029/92JA01139.

Blake, J., P. Carranza, S. Claudepierre, J. Clemmons, J. Crain, W.R., Y. Dotan, J. Fennell, F. Fuentes, R. Galvan, J. George, M. Henderson, M. Lalic, A. Lin, M. Looper, D. Mabry, J. Mazur, B. McCarthy, C. Nguyen, T. OBrien, M. Perez, M. Redding, J. Roeder, D. Salvaggio, G. Sorensen, H. Spence, S. Yi, and M. Zakrzewski (2013), The Magnetic Electron Ion Spectrometer (MagEIS) instruments aboard the Radiation Belt Storm Probes (RBSP) spacecraft, *Space Science Reviews*, 179(1-4), 383–421, doi:10.1007/s11214-013-9991-8.

Blake, J. B., J. F. Fennell, L. M. Friesen, B. M. Johnson, W. A. Kolasinski, D. J. Mabry, J. V. Osborn, S. H. Penzin, E. R. Schnauss, H. E. Spence, D. N. Baker, R. Belian, T. A. Fritz, W. Ford, B. Laubscher, R. Stiglich, R. A. Baraze, M. F. Hilsenrath, W. L. Imhof, J. R. Kilner, J. Mobilia, D. H. Voss, A. Korth, M. Güll, K. Fisher, M. Grande, and D. Hall (1995), CEPPAD, *Space Sci. Rev.*, 71, 531–562, doi:10.1007/BF00751340.

Borovsky, J. E., M. F. Thomsen, D. J. McComas, T. E. Cayton, and D. J. Knipp (1998), Magnetospheric dynamics and mass flow during the november 1993 storm, *Journal of Geophysical Research: Space Physics*, 103(A11), 26,373–26,394, doi:10.1029/97JA03051.



Bourdarie, S., R. H. W. Friedel, J. Fennell, S. Kanekal, and T. E. Cayton (2005), Radiation belt representation of the energetic electron environment: Model and data synthesis using the Salammbô radiation belt transport code and Los Alamos geosynchronous and GPS energetic particle data, *Space Weather*, 3(4), doi:10.1029/2004SW000065, s04S01.

Cayton, T. E. (2004), Monte carlo simulation of the particle channels of the combined X-ray sensor and dosimeter (CXD), *Tech. Rep. LA-UR-04-7092*, Los Alamos National Laboratory, Los Alamos, NM 87545, USA. <http://permalink.lanl.gov/object/tr?what=info:lanl-repo/lareport/LA-UR-04-7092>

Cayton, T. E., and M. Tuszewski (2005), Improved electron fluxes from the Synchronous Orbit Particle Analyzer, *Space Weather*, 3(11), doi:10.1029/2005SW000150, s11B05.

Cayton, T. E., R. D. Belian, S. P. Gary, T. A. Fritz, and D. N. Baker (1989), Energetic electron components at geosynchronous orbit, *Geophysical Research Letters*, 16(2), 147–150, doi:10.1029/GL016i002p00147.

Cayton, T. E., D. M. Drake, K. M. Spencer, M. Herrin, T. J. Wehner, and R. C. Reedy (1998), Description of the BDD–IIR: Electron and proton sensors on the GPS, *Tech. Rep. LA-UR-98-1162*, Los Alamos National Laboratory, Los Alamos, NM 87545, USA, doi:10.2172/674727.

Cherniak, I., I. Zakharenkova, and R. J. Redmon (2015), Dynamics of the high-latitude ionospheric irregularities during the 17 March 2015 St. Patrick's Day storm: Ground-based GPS measurements, *Space Weather*, 13(9), 585–597, doi:10.1002/2015SW001237, 2015SW001237.

Claudepierre, S. G., T. P. O'Brien, J. B. Blake, J. F. Fennell, J. L. Roeder, J. H. Clemmons, M. D. Looper, J. E. Mazur, T. M. Mulligan, H. E. Spence, G. D. Reeves, R. H. W. Friedel, M. G. Henderson, and B. A. Larsen (2015), A background correction algorithm for Van

Allen Probes MagEIS electron flux measurements, *J. Geophys. Res.*, *120*, 5703–5727, doi:10.1002/2015JA021171.

Denton, M. H., and T. E. Cayton (2011), Density and temperature of energetic electrons in the Earth's magnetotail derived from high-latitude GPS observations during the declining phase of the solar cycle, *Annales Geophysicae*, *29*(10), 1755–1763, doi:10.5194/angeo-29-1755-2011.

Distel, J. R., S. G. Blair, T. E. Cayton, R. D. Dingler, F. Guyker, J. C. Ingraham, E. Noveroske, R. C. Reedy, K. M. Spencer, and T. J. Wehner (1999), The combined x-ray dosimeter CXD on GPS block IIR satellites, <http://permalink.lanl.gov/object/tr?what=info:lanl-repo/lareport/LA-UR-99-2280>.

Drake, D. M., T. E. Cayton, P. R. Higbie, D. K. McDaniels, R. C. Reedy, R. Belian, S. A. Walker, L. K. Cope, E. Noveroske, and C. L. Baca (1993), Experimental evaluation of the BDD-I dosimeter for the global positioning system, *Nucl. Instrum. Methods Phys. Res.*, *A333*(2-3), 571–588.

Feldman, W., W. Aiello, D. Drake, and M. Herrin (1985), The BDD II: An improved electron dosimeter for the Global Positioning System, *Tech. Rep. LA-10453-MS*, Los Alamos National Laboratory, Los Alamos, NM 87545, USA.

Fraser-Smith, A. C. (1987), Centered and eccentric geomagnetic dipoles and their poles, 16001985, *Reviews of Geophysics*, *25*(1), 1–16, doi:10.1029/RG025i001p00001.

Friedel, R. H. W., S. Bourdarie, and T. E. Cayton (2005), Intercalibration of magnetospheric energetic electron data, *Space Weather*, *3*(9), doi:10.1029/2005SW000153, s09B04.

Ganushkina, N. Y., I. Dandouras, Y. Y. Shprits, and J. Cao (2011), Locations of boundaries of outer and inner radiation belts as observed by cluster and double star, *Journal of Geophysical*

*Research: Space Physics*, 116(A9), doi:10.1029/2010JA016376, a09234.

Ginet, G. P., T. P. O'Brien, S. L. Huston, W. R. Johnston, T. B. Guild, R. Friedel, C. D. Lindstrom, C. J. Roth, P. Whelan, R. A. Quinn, D. Madden, S. Morley, and Y.-J. Su (2013), AE9, AP9 and SPM: New Models for Specifying the Trapped Energetic Particle and Space Plasma Environment, *Space Sci. Rev.*, 179, 579–615, doi:10.1007/s11214-013-9964-y.

Hilton, H. H. (1971), L parameter, a new approximation, *Journal of Geophysical Research*, 76(28), 6952–6954, doi:10.1029/JA076i028p06952.

Horne, R. B., and D. Pitchford (2015), Space weather concerns for all-electric propulsion satellites, *Space Weather*, 13(8), 430–433, doi:10.1002/2015SW001198, 2015SW001198.

Ingraham, J. C., T. E. Cayton, R. D. Belian, R. A. Christensen, F. Guyker, M. M. Meier, G. D. Reeves, D. H. Brautigam, M. S. Gussenhoven, and R. M. Robinson (1996), Multi-satellite characterization of the large energetic electron flux increase at L=4–7, in the five-day period following the March 24, 1991, solar energetic particle event, in *Workshop on the Earth's trapped particle environment*, edited by G. D. Reeves, pp. 103–108, American Institute of Physics.

James, F., and M. Roos (1975), Minuit - a system for function minimization and analysis of the parameter errors and correlations, *Computer Physics Communications*, 10(6), 343–367, doi:http://dx.doi.org/10.1016/0010-4655(75)90039-9.

Johnston, W. R., C. D. Lindstrom, and G. P. Ginet (2010), Characterization of radiation belt electron energy spectra from CRRES observations, *AGU Fall Meeting Abstracts*, p. C1925.

Kellerman, A. C., Y. Y. Shprits, D. Kondrashov, D. Subbotin, R. A. Makarevich, E. Donovan, and T. Nagai (2014), Three-dimensional data assimilation and reanalysis of radiation belt electrons: Observations of a four-zone structure using five spacecraft and the

verb code, *Journal of Geophysical Research: Space Physics*, 119(11), 8764–8783, doi:10.1002/2014JA020171.

Koller, J., Y. Chen, G. D. Reeves, R. H. W. Friedel, T. E. Cayton, and J. A. Vrugt (2007), Identifying the radiation belt source region by data assimilation, *Journal of Geophysical Research: Space Physics*, 112(A6), doi:10.1029/2006JA012196, a06244.

Li, X., D. N. Baker, M. Temerin, T. E. Cayton, G. D. Reeves, R. S. Selesnick, J. B. Blake, G. Lu, S. G. Kanekal, and H. J. Singer (1999), Rapid enhancements of relativistic electrons deep in the magnetosphere during the May 15, 1997, magnetic storm, *J. Geophys. Res.*, 104(A3), 4467–4476, doi:10.1029/1998JA900092.

Li, X., D. N. Baker, M. Temerin, G. Reeves, R. Friedel, and C. Shen (2005), Energetic electrons, 50 keV to 6 MeV, at geosynchronous orbit: Their responses to solar wind variations, *Space Weather*, 3(4), doi:10.1029/2004SW000105, s04001.

Lohmeyer, W., and K. Cahoy (2013), Space weather radiation effects on geostationary satellite solid-state power amplifiers, *Space Weather*, 11(8), 476–488, doi:10.1002/swe.20071.

Maget, V., S. Bourdarie, D. Boscher, and R. H. W. Friedel (2007), Data assimilation of LANL satellite data into the Salammbô electron code over a complete solar cycle by direct insertion, *Space Weather*, 5(10), doi:10.1029/2007SW000322, s10003.

Mauk, B., N. Fox, S. Kanekal, R. Kessel, D. Sibeck, and A. Ukhorskiy (2013), Science objectives and rationale for the Radiation Belt Storm Probes mission, *Space Science Reviews*, 179(1-4), 3–27, doi:10.1007/s11214-012-9908-y.

McAdams, K. L., G. D. Reeves, R. H. W. Friedel, and T. E. Cayton (2001), Multisatellite comparisons of the radiation belt response to the geospace environment modeling (gem) magnetic storms, *Journal of Geophysical Research: Space Physics*, 106(A6), 10,869–10,882,

doi:10.1029/2000JA000248.

McIlwain, C. E. (1961), Coordinates for mapping the distribution of magnetically trapped particles, *Journal of Geophysical Research*, 66(11), 3681–3691, doi:10.1029/JZ066i011p03681.

Millan, R. M., R. P. Lin, D. M. Smith, and M. P. McCarthy (2007), Observation of relativistic electron precipitation during a rapid decrease of trapped relativistic electron flux, *Geophysical Research Letters*, 34(10), doi:10.1029/2006GL028653, 110101.

Morley, S. K., R. H. W. Friedel, T. E. Cayton, and E. Noveroske (2010a), A rapid, global and prolonged electron radiation belt dropout observed with the Global Positioning System constellation, *Geophys. Res. Lett.*, 37, L06,102, doi:10.1029/2010GL042772.

Morley, S. K., R. H. W. Friedel, E. L. Spanswick, G. D. Reeves, J. T. Steinberg, J. Koller, T. E. Cayton, and E. Noveroske (2010b), Dropouts of the outer electron radiation belt in response to solar wind stream interfaces: global positioning system observations, *Proc. Royal Society A*, 466, 3329–3350, doi:10.1098/rspa.2010.0078.

Morley, S. K., M. G. Henderson, G. D. Reeves, R. H. W. Friedel, and D. N. Baker (2013), Phase space density matching of relativistic electrons using the van allen probes: Rept results, *Geophysical Research Letters*, 40(18), 4798–4802, doi:10.1002/grl.50909.

Morley, S. K., J. P. Sullivan, R. C. Schirato, and J. R. Terry (2014), Data processing for energetic particle measurements from the Global Positioning System constellation, *Tech. Rep. LA-UR-14-28961*, Los Alamos National Laboratory, Los Alamos, NM 87545, USA, doi:10.2172/1164428.

O'Brien, T. P., S. G. Claudepierre, M. D. Looper, J. B. Blake, J. F. Fennell, J. H. Clemmons, J. L. Roeder, S. G. Kanekal, J. W. Manweiler, D. G. Mitchell, M. Gkioulidou, L. J. Lanzerotti, H. E. Spence, G. D. Reeves, and D. N. Baker (2015), On the use of drift echoes to characterize on-

orbit sensor discrepancies, *J. Geophys. Res.*, *120*(3), 2076–2087, doi:10.1002/2014JA020859, 2014JA020859.

Press, W. H., S. A. Teukolsky, W. T. Vetterling, and B. P. Flannery (1992), *Numerical recipes in C: The art of scientific computing*, Cambridge University Press.

Reeves, G. D., Y. Chen, G. S. Cunningham, R. W. H. Friedel, M. G. Henderson, V. K. Jordanova, J. Koller, S. K. Morley, M. F. Thomsen, and S. Zaharia (2012), Dynamic radiation environment assimilation model: Dream, *Space Weather*, *10*(3), doi:10.1029/2011SW000729, s03006.

Reeves, G. D., H. E. Spence, M. G. Henderson, S. K. Morley, R. H. W. Friedel, H. O. Funsten, D. N. Baker, S. G. Kanekal, J. B. Blake, J. F. Fennell, S. G. Claudepierre, R. M. Thorne, D. L. Turner, C. A. Kletzing, W. S. Kurth, B. A. Larsen, and J. T. Niehof (2013), Electron Acceleration in the Heart of the Van Allen Radiation Belts, *Science*, *341*(6149), 991–994, doi:10.1126/science.1237743.

Rozanov, E., M. Calisto, T. Egorova, T. Peter, and W. Schmutz (2012), Influence of the precipitating energetic particles on atmospheric chemistry and climate, *Surveys in Geophysics*, *33*(3-4), 483–501, doi:10.1007/s10712-012-9192-0.

Sen, P. K. (1968), Estimates of the regression coefficient based on Kendall's Tau, *Journal of the American Statistical Association*, *63*(324), 1379–1389, doi:10.1080/01621459.1968.10480934.

Sheskin, D. J. (2007), *Handbook of Parametric and Nonparametric Statistical Procedures, Fourth Edition*, Chapman and Hall/CRC.

Shue, J. H., J. K. Chao, H. C. Fu, C. T. Russell, P. Song, K. K. Khurana, and H. J. Singer (1997), A new functional form to study the solar wind control of the magnetopause size and shape, *J.*

*Geophys. Res.*, 102, 9497–9511.

- Spence, H. E., G. D. Reeves, D. N. Baker, J. B. Blake, M. Bolton, S. Bourdarie, A. A. Chan, S. G. Claudepierre, J. H. Clemmons, J. P. Cravens, S. R. Elkington, J. F. Fennell, R. H. W. Friedel, H. O. Funsten, J. Goldstein, J. C. Green, A. Guthrie, M. G. Henderson, R. B. Horne, M. K. Hudson, J.-M. Jahn, V. K. Jordanova, S. G. Kanekal, B. W. Klatt, B. A. Larsen, X. Li, E. A. MacDonald, I. R. Mann, J. Niehof, T. P. O'Brien, T. G. Onsager, D. Salvaggio, R. M. Skoug, S. S. Smith, L. L. Suther, M. F. Thomsen, and R. M. Thorne (2013), Science goals and overview of the Radiation Belt Storm Probes (RBSP) Energetic particle, Composition, and Thermal plasma (ECT) suite on NASA's Van Allen Probes mission, *Space Science Reviews*, 179(1-4), 311–336, doi:10.1007/s11214-013-0007-5.
- Taylor, M. G. G. T., R. H. W. Friedel, G. D. Reeves, M. W. Dunlop, T. A. Fritz, P. W. Daly, and A. Balogh (2004), Multisatellite measurements of electron phase space density gradients in the Earth's inner and outer magnetosphere, *Journal of Geophysical Research: Space Physics*, 109(A5), doi:10.1029/2003JA010294, a05220.
- Tsyganenko, N. A. (1989), A magnetospheric magnetic field model with a warped tail current sheet, *Planet. Space Sci.*, 37, 5–20, doi:10.1016/0032-0633(89)90066-4.
- Tukey, J. W. (1977), *Exploratory Data Analysis*, Addison-Wesley.
- Turner, D. L., V. Angelopoulos, S. K. Morley, M. G. Henderson, G. D. Reeves, W. Li, D. N. Baker, C.-L. Huang, A. Boyd, H. E. Spence, S. G. Claudepierre, J. B. Blake, and J. V. Rodriguez (2014), On the cause and extent of outer radiation belt losses during the 30 September 2012 dropout event, *Journal of Geophysical Research: Space Physics*, 119(3), 1530–1540, doi:10.1002/2013JA019446, 2013JA019446.

- Turunen, E., P. T. Verronen, A. Seppälä, C. J. Rodger, M. A. Clilverd, J. Tamminen, C.-F. Enell, and T. Ulich (2009), Impact of different energies of precipitating particles on NO<sub>x</sub> generation in the middle and upper atmosphere during geomagnetic storms, *J. Atmos. Sol.-Terr. Phys.*, **71**, 1176–1189, doi:10.1016/j.jastp.2008.07.005.
- Tuszewski, M., T. E. Cayton, J. C. Ingraham, and R. M. Kippen (2004), Bremsstrahlung effects in energetic particle detectors, *Space Weather*, **2**(10), doi:10.1029/2003SW000057, s10S01.
- Vampola, A. L., J. V. Osborne, and B. M. Johnson (1992), CRRES magnetic electron spectrometer AFGL-701-5A (MEA), *J. Spacecr. Rockets*, **29**, 592–594.
- Vassiliadis, D., A. J. Klimas, R. S. Weigel, D. N. Baker, E. J. Rigler, S. G. Kanekal, T. Nagai, S. F. Fung, R. W. H. Friedel, and T. E. Cayton (2003), Structure of Earth's outer radiation belt inferred from long-term electron flux dynamics, *Geophysical Research Letters*, **30**(19), doi:10.1029/2003GL017328, 2003.
- Welling, D. T. (2010), The long-term effects of space weather on satellite operations, *Ann. Geophys.*, **28**(6), 1361–1367, doi:10.5194/angeo-28-1361-2010.
- Wilcox, R. R. (1998), How many discoveries have been lost by ignoring modern statistical methods?, *American Psychologist*, **53**, 300–314.
- Wilks, D. S. (2006), *Statistical methods in the atmospheric sciences, 2nd Edition*, Academic Press.
- Yu, Y., J. Koller, and S. K. Morley (2013), Quantifying the effect of magnetopause shadowing on electron radiation belt dropouts, *Annales Geophysicae*, **31**(11), 1929–1939, doi:10.5194/angeo-31-1929-2013.



**Table 1.** Selected details of Global Positioning System satellites carrying Los Alamos Combined X-Ray Dosimeters (CXD) used in this study. The columns give, in order, the NORAD tracking number, the space vehicle number, the international designation, the orbital plane, block and the date from which CXD data are available. Expanded from table 1 of *Morley et al.* [2010b]

| NORAD # | SVN  | ID        | Orbit. Plane | Block | Data From (mm/yy) |
|---------|------|-----------|--------------|-------|-------------------|
| 40730   | ns72 | 2015-033A | C            | IIF   | 08/2015           |
| 40534   | ns71 | 2015-013A | B            | IIF   | 04/2015           |
| 40294   | ns69 | 2014-068A | E            | IIF   | 12/2014           |
| 40105   | ns68 | 2014-045A | F            | IIF   | 09/2014           |
| 39741   | ns67 | 2014-026A | D            | IIF   | 07/2014           |
| 39533   | ns64 | 2014-008A | A            | IIF   | 05/2014           |
| 39166   | ns66 | 2013-023A | C            | IIF   | 07/2013           |
| 38833   | ns65 | 2012-053A | A            | IIF   | 11/2012           |
| 37753   | ns63 | 2011-036A | D            | IIF   | 10/2011           |
| 36585   | ns62 | 2010-022A | B            | IIF   | 06/2010           |
| 32384   | ns57 | 2007-062A | C            | IIR-M | 01/2008           |
| 32260   | ns55 | 2007-047A | F            | IIR-M | 11/2007           |
| 29601   | ns58 | 2006-052A | B            | IIR-M | 12/2006           |
| 28874   | ns53 | 2005-038A | C            | IIR-M | 10/2005           |
| 28474   | ns61 | 2004-045A | D            | IIR   | 11/2004           |
| 28361   | ns60 | 2004-023A | F            | IIR   | 07/2004           |
| 28190   | ns59 | 2004-009A | C            | IIR   | 03/2004           |
| 27663   | ns56 | 2003-005A | B            | IIR   | 02/2003           |
| 26690   | ns54 | 2001-004A | E            | IIR   | 02/2001           |

**Table 2.** Nominal energy channel assignments for CXD instrument and scaling on previously published response functions [cf. *Cayton, 2004; Morley et al., 2014*].

| Channel | Nominal Energy [MeV] | Response Scaling |           |
|---------|----------------------|------------------|-----------|
|         |                      | Block IIR/IIR-M  | Block IIF |
| 1       | 0.14 - 0.23          | 1.61             | 1.08      |
| 2       | 0.23 - 0.41          | 1.45             | 1.00      |
| 3       | 0.41 - 0.77          | 1.40             | 1.00      |
| 4       | 0.77 - 1.25          | 1.25             | 0.93      |
| 5       | 1.26 -               | 1.40             | 1.00      |
| 6       | 1.3 - 1.7            | 1.00             | 0.70      |
| 7       | 1.7 - 2.2            | 0.84             | 0.77      |
| 8       | 2.2 - 3.0            | 0.74             | 1.00      |
| 9       | 3.0 - 4.1            | 1.00             | 1.00      |
| 10      | 4.1 - 5.8            | 1.00             | 1.00      |
| 11      | 5.8 -                | 1.00             | 1.00      |

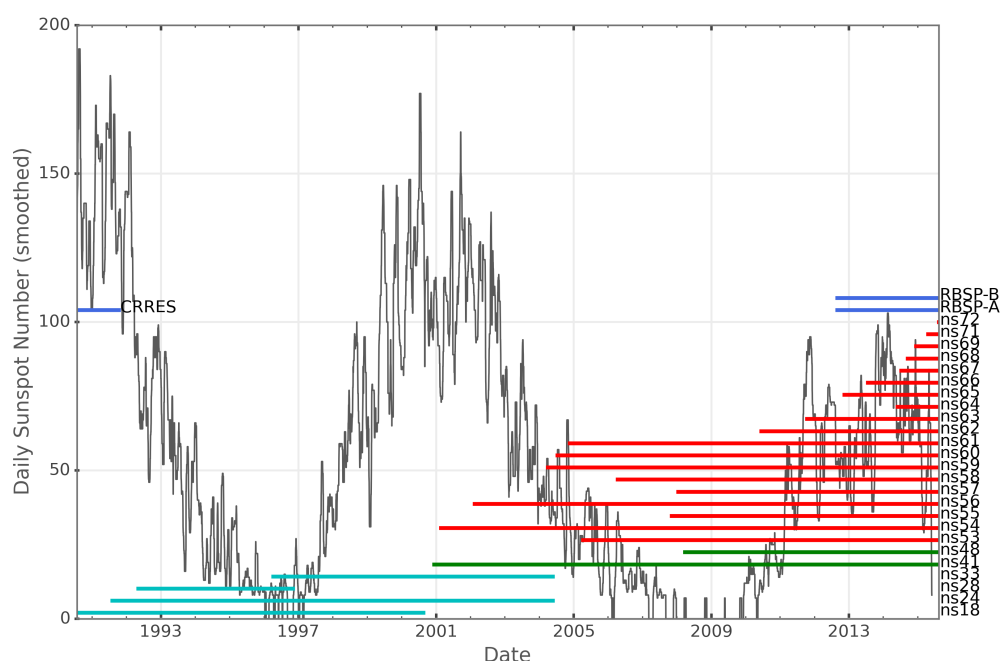


**Figure 1.** The temporal coverage of selected missions flying energetic electron detectors from July 1990 to August 2015. The daily sunspot number is given by the dark grey line to show the context within the solar cycle. The colored horizontal bars show the data coverage for each satellite; these bars are individually annotated with the satellite name. The dark blue bars show the “gold standard” radiation belt missions: CRRES (1990-1991) and Van Allen Probes (2012-). The red bars mark the coverage of the CXD-equipped GPS satellites. The green bars mark the coverage of the BDD-IIR instrumented GPS satellites and the cyan bars show the coverage of the older BDD-II series detectors.

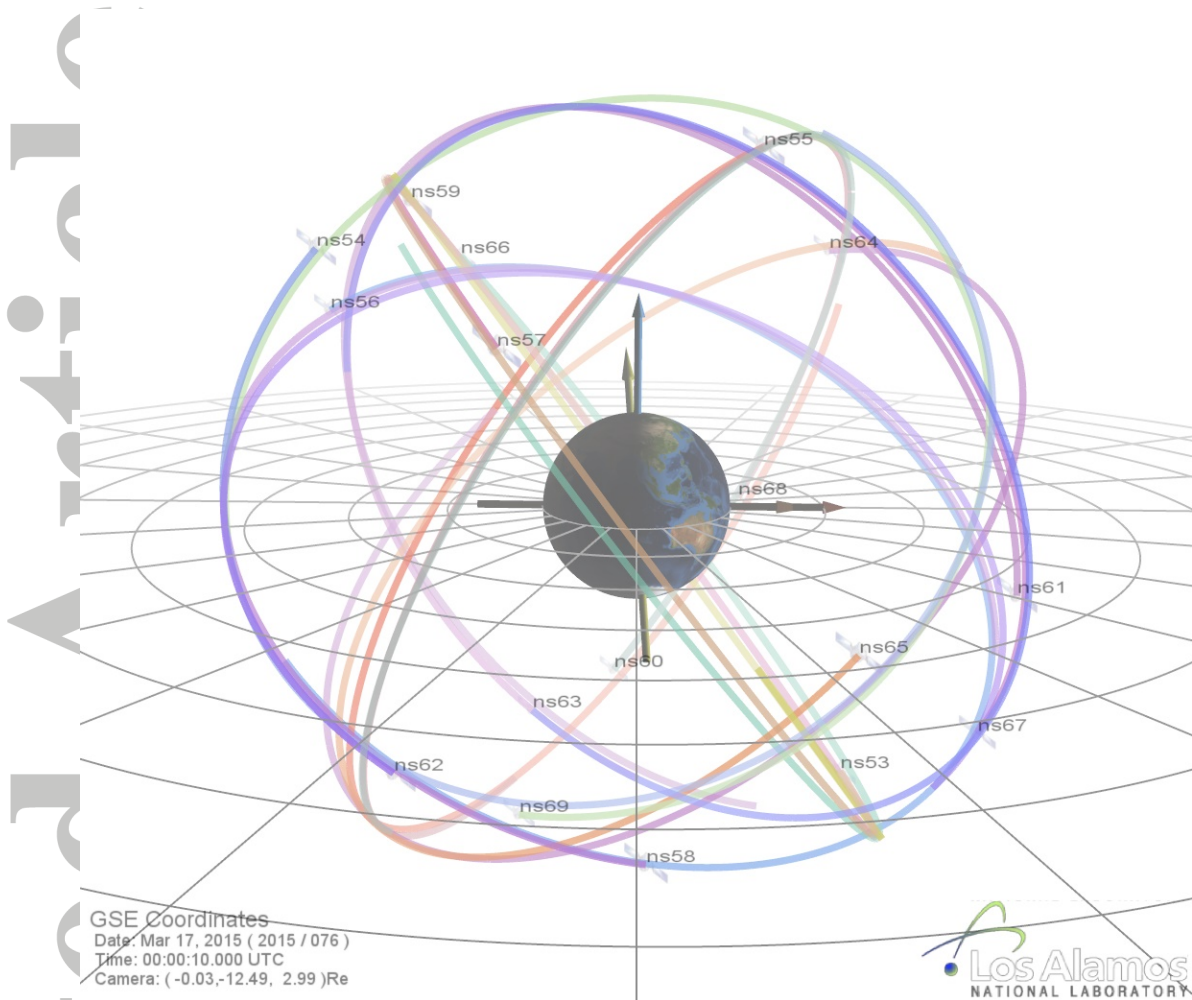


**Figure 2.** A visualization, in Geocentric Solar Ecliptic (GSE) coordinates, of the orbits of the CXD-equipped GPS satellites listed in table 1, at midnight on March 17th 2015. The satellite names mark the location of each satellite at this time and the orbital track for the previous 12 hours is shown in color. The colors fade with both distance from the viewpoint and with the time since the satellite was at that location. The orange and red arrows mark the Earth-Sun vector and GSE X-vector. The GSE Z-vector is marked by the blue arrow and the green arrow marks the dipole axis. The grid is in the GSE equatorial plane (i.e. the ecliptic plane).

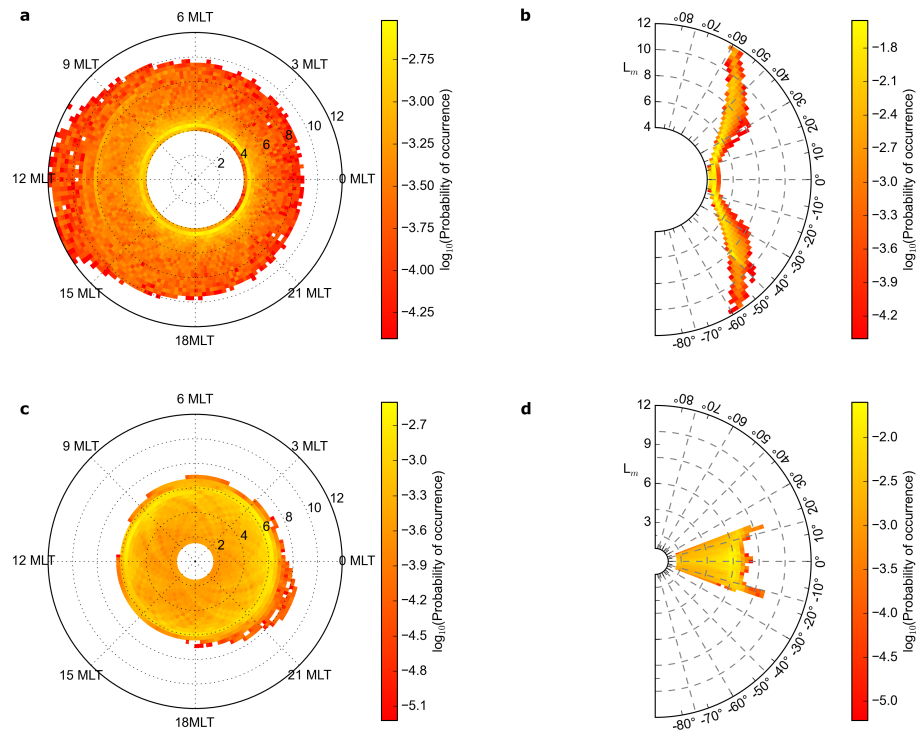


**Figure 3.** The spatial sampling of a representative GPS satellite (ns65) and Van Allen probes satellite RBSP-A, represented by the logarithm of the probability of occurrence for each bin. Panels a (ns65) and c (RBSP-A) show the sampling in Magnetic Local Time as a function of McIlwain L. Panels b (ns65) and d (RBSP-A) show the sampling in magnetic latitude as a function of McIlwain L.

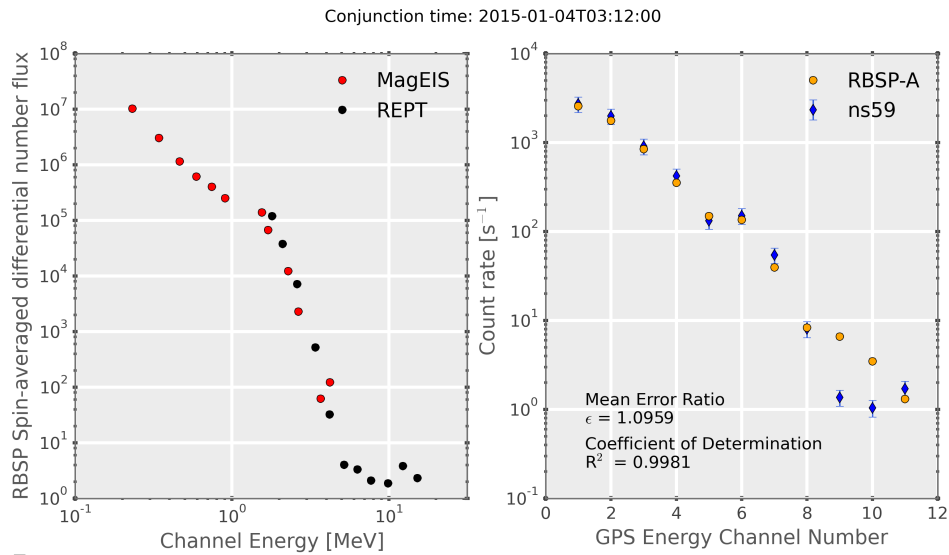


**Figure 4.** A two-panel plot showing: (left) spin-averaged electron number flux measured by Van Allen Probes, where data from MagEIS are colored red and REPT data are colored black; (right) a comparison of the count rates in each GPS electron energy channel, where the GPS count rates are colored blue and the “expected” count rate from Van Allen Probes are colored orange. The “expected” counts are derived by folding the observed flux spectrum with the CXD response function. Metrics for the correspondence between the count rates are displayed in the right-hand panel.

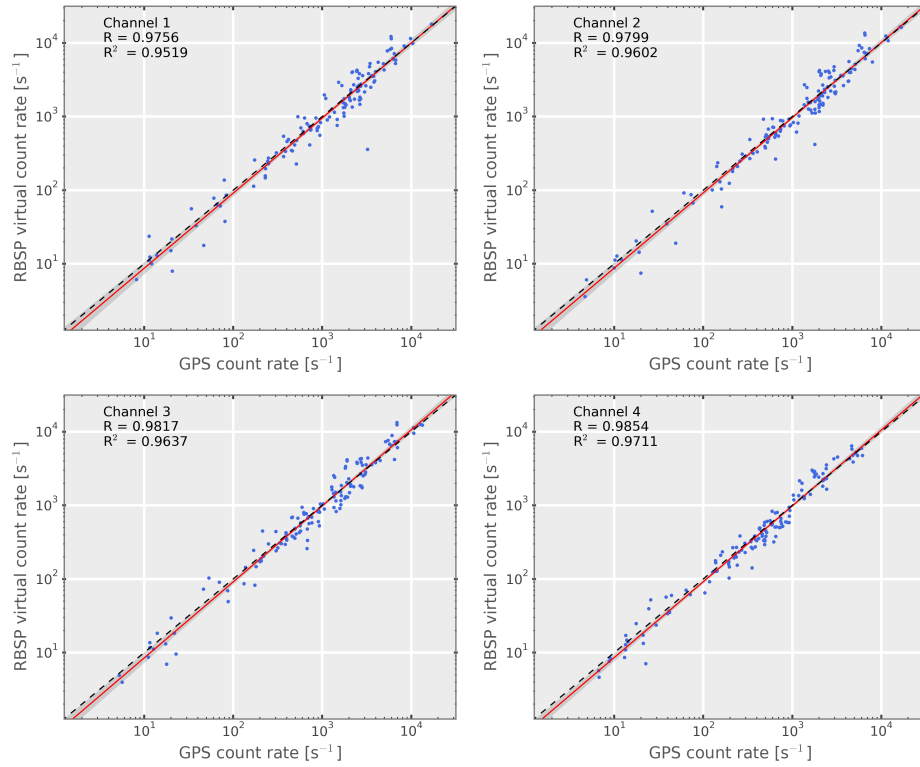


**Figure 5.** Scatter plots of the measured and “expected” count rates for all conjunctions for GPS energy channels 1 through 4. The dashed black lines show  $y = x$ , the red lines are the best fits to the data and the grey envelopes mark the 95% confidence interval on the linear fit.

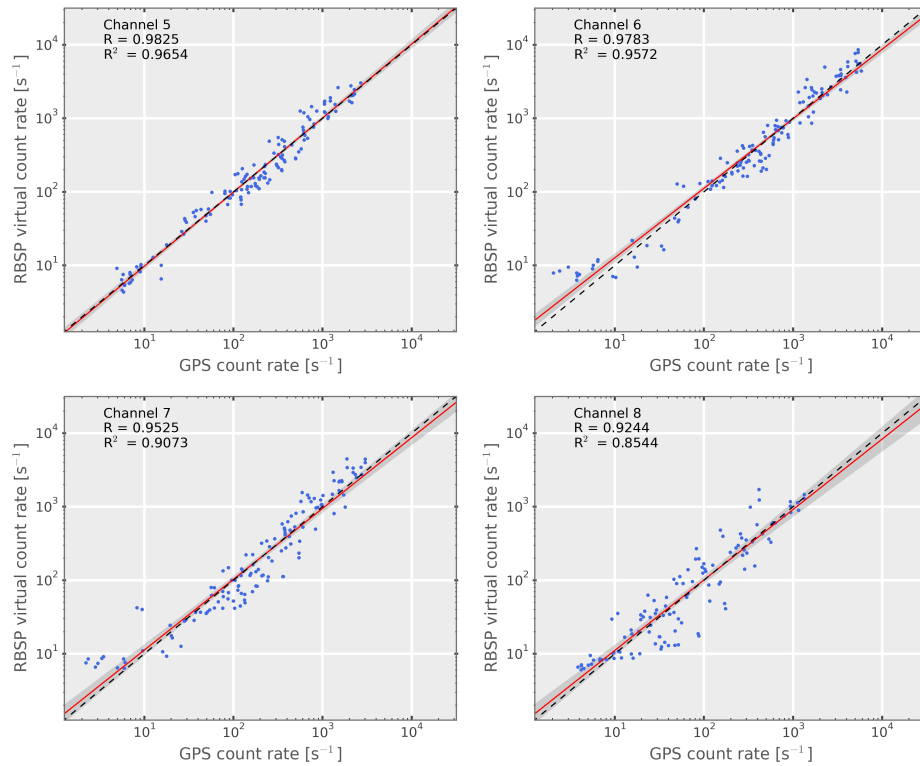


**Figure 6.** Scatter plots of the measured and “expected” count rates for all conjunctions for GPS energy channels 5 through 8. The format is identical to figure 5.



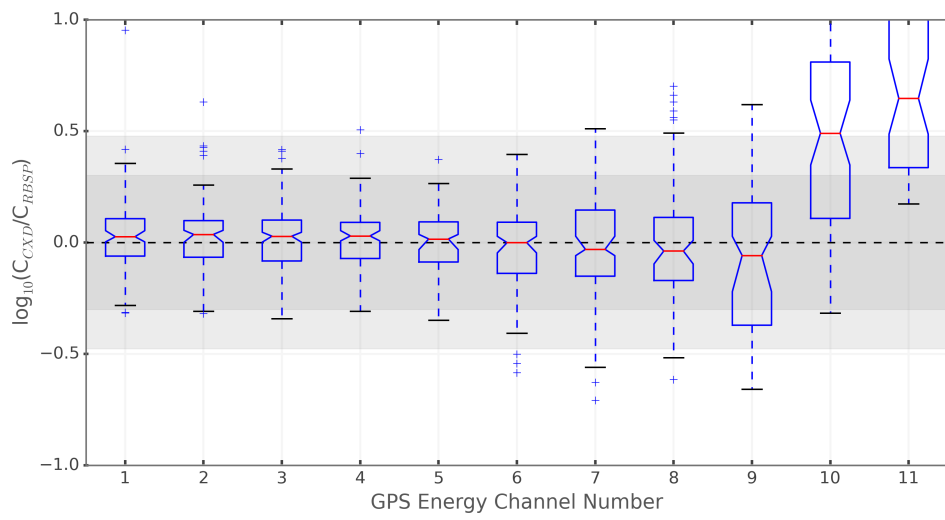


**Figure 7.** Boxplots of the  $\log_{10}$  of the ratio of measured to “expected” count rates for all conjunctions for all GPS electron energy channels.

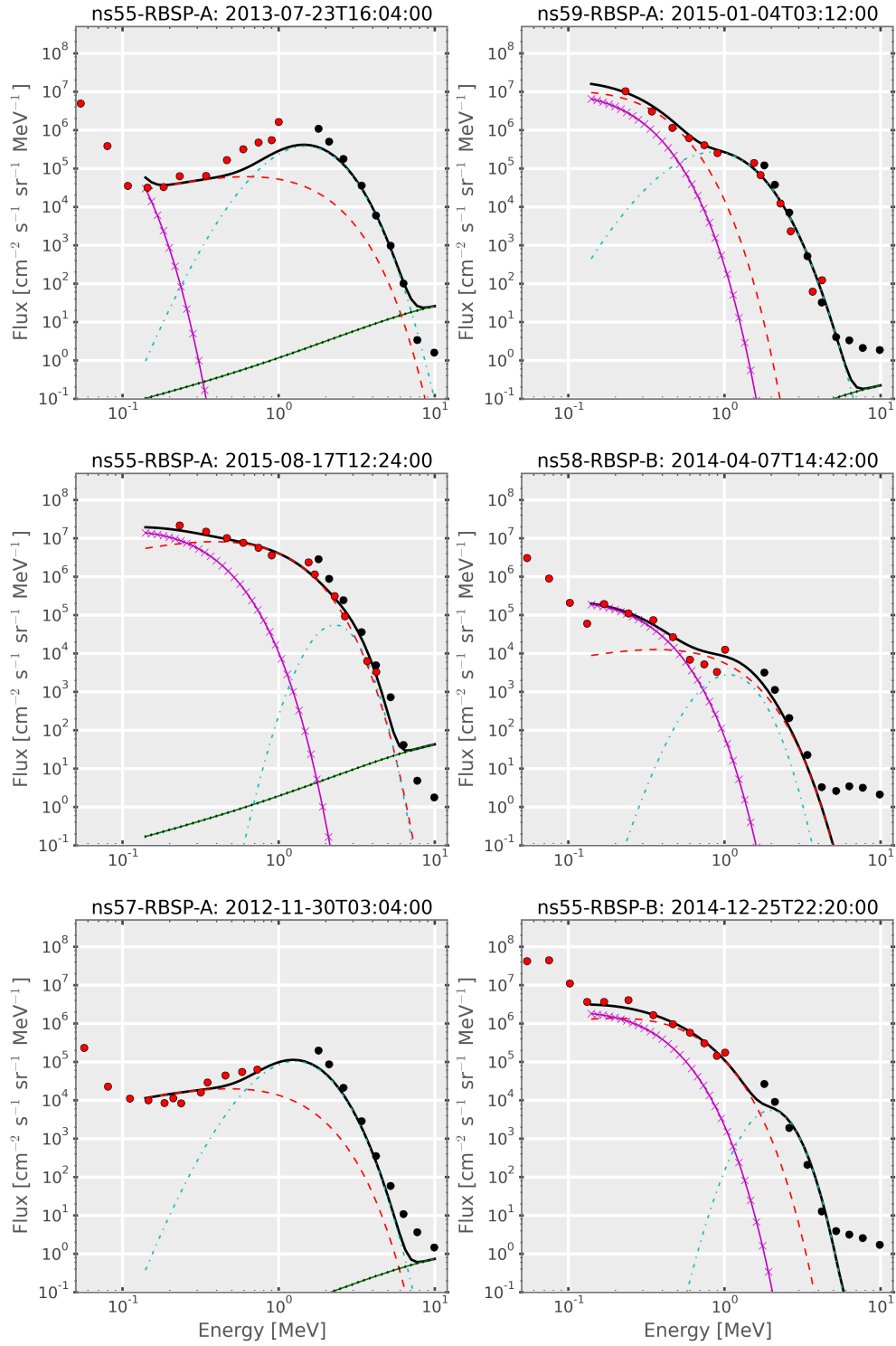


**Figure 8.** Sample spectra calculated from the CXD count rates (black lines) compared with contemporaneous measurements from the Van Allen Probes (solid markers). The red circles mark data from MageIS and the black circles mark data from REPT. The component distributions used in fitting the flux are shown by the colored lines and are fully described in the text. Each panel has the date and time of the conjunction, with the satellite names, in the title.

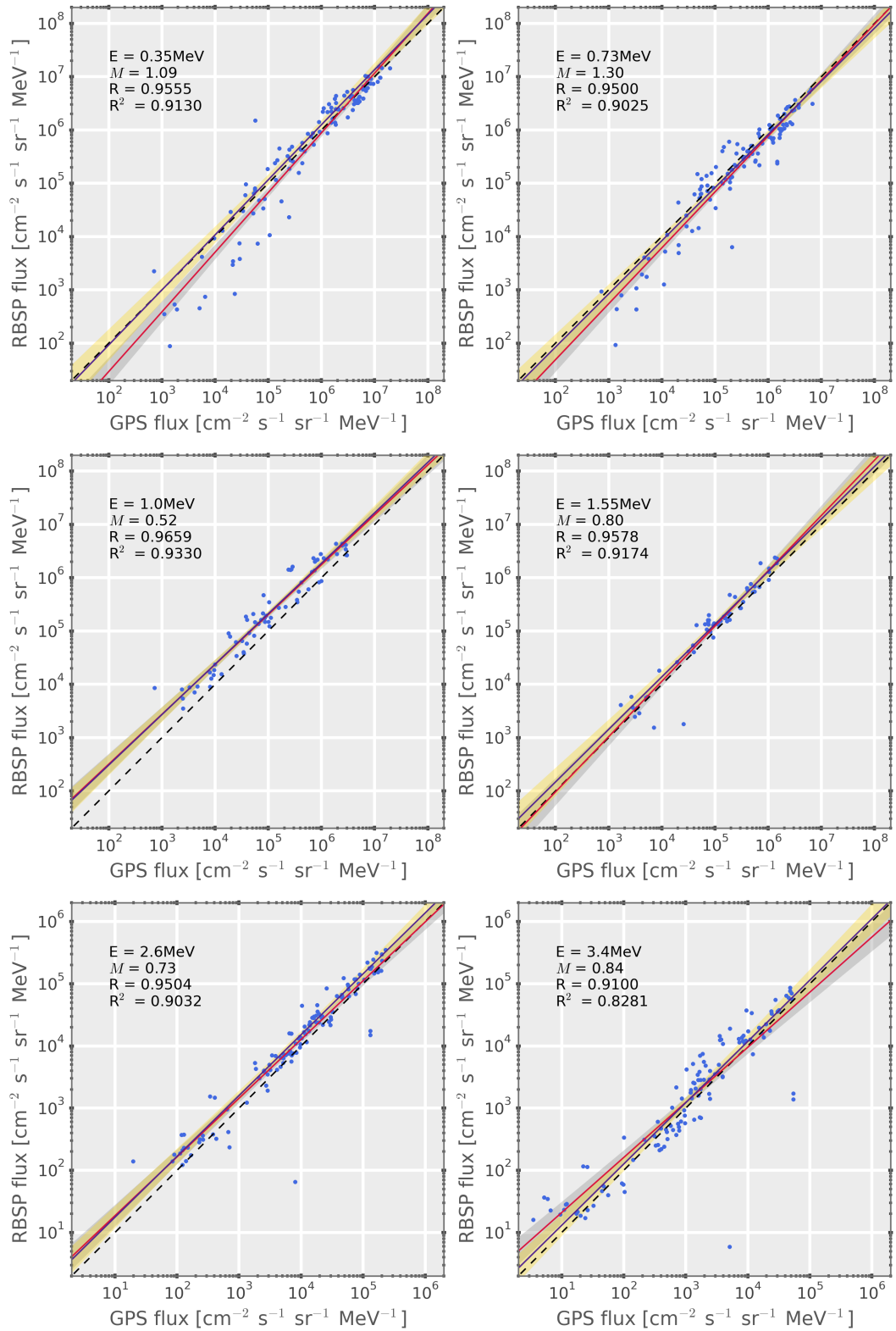


**Figure 9.** Scatter plots of the GPS electron fluxes and RBSP electron fluxes for six energies. The format is similar to figure 5, with the addition of an annotated bias (median ratio of fluxes) and an additional linear fit. The purple line gives a robust linear fit, calculated using the Theil-Sen estimator, with a 95% confidence interval marked in yellow.

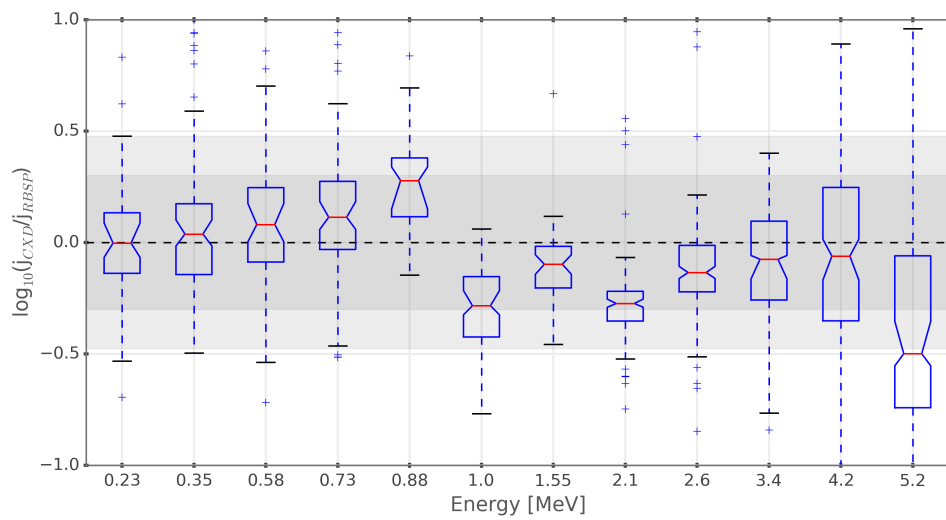


**Figure 10.** Boxplots of the  $\log_{10}$  of the ratio of GPS electron fluxes to RBSP electron fluxes for 12 energies. The dark shaded region marks a factor of 2 difference and the light shaded region marks a factor of 3 difference.

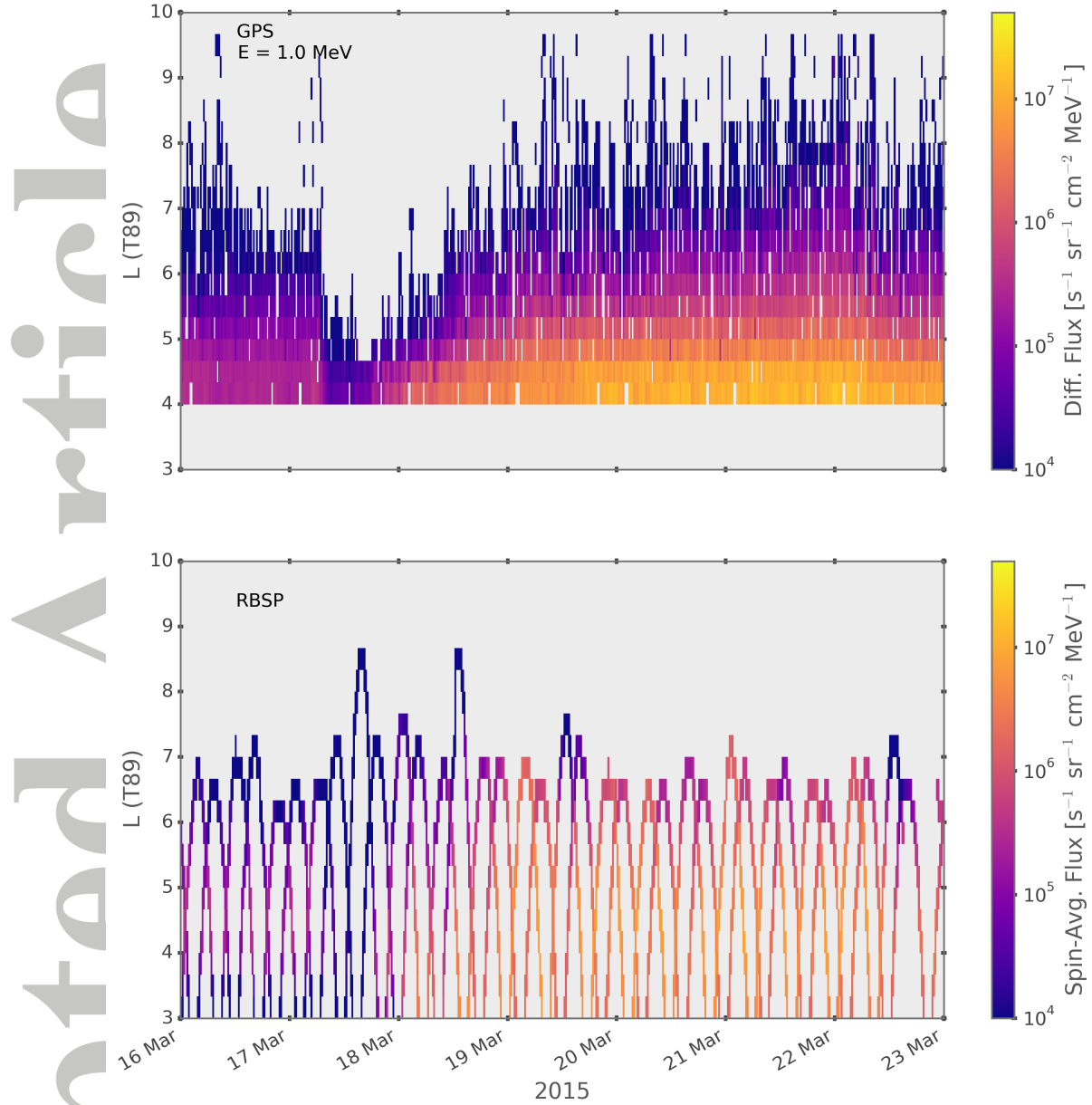


**Figure 11.** The upper panel shows 1 MeV differential electron flux measured by the GPS CXD instruments, sorted by McIlwain L (calculated using T89). The lower panel shows  $\approx 1$  MeV spin-averaged electron flux measured by the MagEIS instruments on Van Allen Probes. The data are binned averages with a temporal resolution of 20 minutes and a resolution of  $1/3$  in L. Data from 17 GPS satellites were combined to make the upper panel; data from both RBSP-A and RBSP-B are included in the lower panel.